

IMPLEMENTING ADVANCED POWER QUALITY AND EFFICIENCY SOLUTIONS IN INDUSTRY 4.0: THE ROLE OF DYNAMIC LOAD BALANCING AND POWER FACTOR CORRECTION

YOUSSEF ZERGUIT¹, YOUNES HAMMOUDI², MOSTAFA DERRHI³

^{1,3}LTI Research Laboratory, ENSAT, Abdelmalek Essaadi University, Tangier, Morocco

²LAMON2E Research Laboratory, FSO, Mohammed First University, Oujda, Morocco

E-mail : ¹youssef.zerguit@etu.uac.ac.ma, ²y.hammoudi@ump.ac.ma, ³m.derrhi@uae.ac.ma

ABSTRACT

The advancement of Industry 4.0 has ushered in a new era of smart industrial operations, driven by the integration of cutting-edge technologies. In this context, we present a pioneering solution that addresses the pivotal aspects of real-time dynamic load balancing and precision power factor correction in three-phase power systems. By harnessing the capabilities of Industry 4.0, our approach optimizes energy consumption while enhancing power quality. Our proposed system synergizes dynamic load balancing with efficient power factor correction in real-time, ensuring optimal distribution of loads and accurate compensation of power factors. This dynamic adaptation minimizes energy wastage and augments power utilization efficiency. The real-time nature of our solution empowers immediate adjustments, facilitating seamless response to varying load conditions. The key advantages of our approach encompass not only energy savings and enhanced power factor but also the integration of Industry 4.0 principles for predictive maintenance and data-driven decision-making. Consequently, industrial processes attain heightened responsiveness, cost-effectiveness, and environmental sustainability. In summary, this paper introduces an innovative contribution aligned with the Industry 4.0 paradigm. By providing real-time solutions for dynamic load balancing and power factor correction, our work enhances both energy efficiency and power quality, ultimately driving smarter and more resource-efficient industrial practices.

Keywords: *Automatic Balancing System, Power Factor Correction, Energy Efficiency, Power Quality, Three-Phase Loads, Three-Phase Balancing, Industry 4.0.*

1. INTRODUCTION

The advent of Industry 4.0 has catalyzed a transformative shift in industrial operations, propelled by the fusion of advanced technologies and data-centric paradigms [1], [2]. This evolution heralds the era of smart factories, where real-time optimization, connectivity, and automation converge to redefine manufacturing processes [3]–[6]. Amidst this transformation, the imperative of energy efficiency and power quality optimization emerges as pivotal to sustainable and cost-effective industrial practices.

Within the framework of Industry 4.0, the challenge of real-time energy efficiency and power quality optimization assumes heightened importance. The dynamic and heterogeneous nature of modern industrial operations results in varying energy consumption patterns and power factor discrepancies across loads [7]–[9]. This dynamic

disparity in energy consumption and power factor demand necessitates a solution capable of dynamically redistributing loads and performing power factor correction in real-time.

The motivation driving this research is twofold—economic and environmental. Inefficient energy utilization not only incurs substantial operational costs but also contributes to a larger ecological footprint. Moreover, compromised power quality can disrupt manufacturing processes and undermine operational efficiency [10], [11]. Existing solutions often lack the agility required to adapt to rapidly changing energy demands and power factor fluctuations. There is still a lot of room for improvement when it comes to figuring out how to apply Industry 4.0 concepts to energy management systems.

This research aims to design, develop, and validate a comprehensive solution that seamlessly integrates real-time load balancing and power factor

correction in Industry 4.0 contexts. The study seeks to demonstrate that by dynamically redistributing loads and performing real-time power factor correction, substantial energy savings can be achieved while maintaining optimal power quality. The research makes a significant contribution by offering an integrated framework that leverages Industry 4.0 technologies, prioritizes real-time adaptability, and aligns with the imperatives of sustainable manufacturing.

The scope of this research encompasses the design and implementation of a Power Monitoring and Control Unit (PMCU) system capable of achieving real-time load balancing and power factor correction. The methodology involves the integration of Industrial Internet of Things (IIoT) devices, enabling continuous monitoring of power parameters and facilitating immediate decision-making. The PMCU interfaces with a Main Control Unit (MCU) and a Main Power Monitoring Unit (MPMU), ensuring synchronized communication and coordinated action. This paper delves into the technical architecture, algorithmic intricacies, and practical deployment of the proposed system.

In the following sections, this paper delves into the historical evolution of unbalanced systems, offers a comprehensive analysis of existing literature, presents an innovative methodology for addressing these systems, shares research outcomes with insightful discussions, and concludes by summarizing key findings and contributions.

2. BACKGROUND

2.1 Industry 4.0 and the Industrial Internet of Things (IIoT)

In 2011, a consortium of German economic experts introduced the term "Industry 4.0" to characterize the fourth industrial revolution. This transformative revolution is propelled by a convergence of cutting-edge technologies, including the Internet of Things (IoT) [12], advanced data analytics, Artificial Intelligence (AI) [13], and additive manufacturing (3D printing). These technologies collaboratively propel the evolution of traditional factories into intelligent entities, where machines communicate seamlessly with both each other and humans, while also autonomously making informed decisions [2].

At the heart of Industry 4.0 lies the concept of the Industrial Internet of Things (IIoT), which applies IoT principles to the realm of manufacturing and other industrial domains. The IIoT facilitates real-time communication and decision-making by interconnecting machines, individuals, data, and

processes [14]. This interconnectedness is accomplished through the deployment of internet-connected sensors and actuators capable of seamless communication [15]. Already, the Industrial Internet of Things (IIoT) is revolutionizing manufacturing through real-time process monitoring and optimization. In the future, it is poised to enable personalized mass production and usher in novel business models [5].

The implementation of Industry 4.0 technologies is anticipated to infuse the manufacturing sector with heightened flexibility, agility, and responsiveness. Furthermore, these technologies are poised to increase efficiency and productivity while concurrently driving down operational costs. Three-Phase System.

2.2 Three-Phase System

Within a three-phase system, electrical currents traverse three distinct wires, accompanied by a neutral wire tasked with conducting fault currents to the ground. This configuration designates three wires for the purposes of power generation, transmission, and distribution. When transitioning to single-phase operation, one of the three phases along with the neutral wire can be isolated. Notably, the cumulative current from the trio of phases results in an equilibrium of zero, with their respective phases spanning a separation of 120° (as visually depicted in Figure 1) [16].

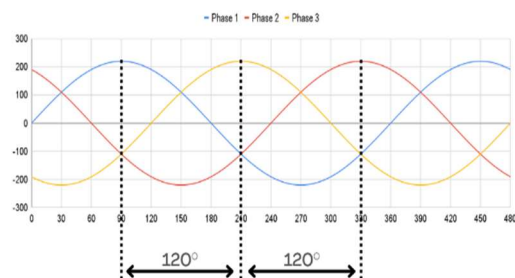


Figure 1: Waveform of a Three-Phase System.

2.3 Three-Phase Balanced and Unbalanced System/Load

A balanced three-phase system is defined by its consistent magnitudes across the three phases, each separated by 120 degrees in terms of phase angles [17], [18]. The system's configuration can either retain this balance or deviate into an unbalanced state, depending on the load conditions [19]. The current dynamics within this three-phase system are encapsulated by (1), representing the phase currents (I_1 , I_2 , and I_3) in relation to their respective peak values, where (α_1 , α_2 , α_3) signify

the phase shift angles. To further elucidate, Table 1 provides a comprehensive breakdown of peak current values and phase shift angles for each phase across various system states. Importantly, Figures 2, 3 and 4 visually enhances understanding by illustrating the load's performance under different scenarios. This figures encapsulates schematic diagrams showcasing a balanced load, magnitude unbalanced load, and phase angle unbalanced load, alongside waveform plots that vividly depict the current characteristics for each load condition. These visual aids collectively offer profound insights into the load's behavior and performance across a spectrum of system states.

$$I_{(1,2,3)} = I_{(1,2,3)peak} * \sin(\theta + \alpha_{(1,2,3)}) \quad (1)$$

Table 1. Peak Current Values and Phase Shift Angles for Different System States.

System State	I_{1peak}	I_{2peak}	I_{3peak}	α_1	α_2	α_3
Balanced	I_{peak}	I_{peak}	I_{peak}	0	$2\pi/3$	$-2\pi/3$
Magnitude Unbalance	I_{1peak}	I_{2peak}	I_{3peak}	0	$2\pi/3$	$-2\pi/3$
Phase Angle Unbalance	I_{peak}	I_{peak}	I_{peak}	α_1	α_2	α_3

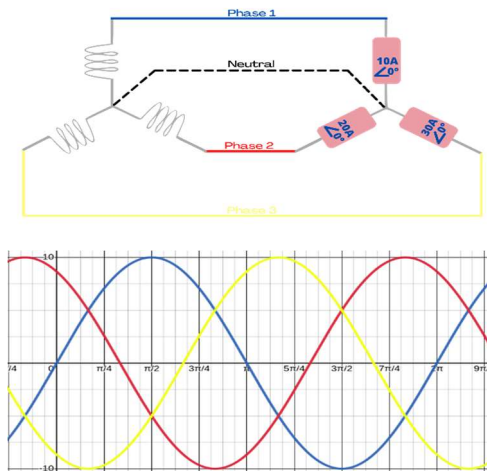


Figure 2: Load Behavior and Current Characteristics in Balanced System.

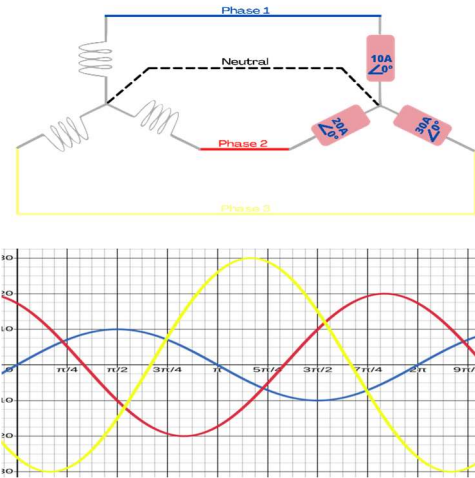


Figure 3: Load Behavior and Current Characteristics in Magnitude Unbalanced System.

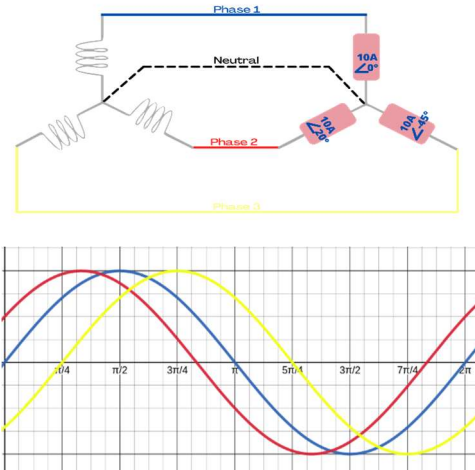


Figure 4: Load Behavior and Current Characteristics in Phase Angle Unbalanced System.

3. RELATED WORKS

In the domain of three-phase power systems, the interplay between dynamic load balancing and efficient power factor correction has garnered considerable attention. This section presents an overview of existing research in these domains and highlights their synergistic potential when combined.

3.1 Dynamic Load Balancing in Three-Phase Systems

Leger et al. [20] proposed an innovative load management system tailored for tactical microgrids. By redistributing loads among phases, their architecture achieved load shedding and balancing, ensuring uninterrupted operation even during load transitions. Laboratory tests of their 208/120 V 14.4 kVA prototype demonstrated rapid

load transition capabilities, offering potential benefits to microgrid performance and control.

Haq et al. [21] introduced an automated balancing system for household loads. Utilizing a microcontroller and relay-based hardware, their system intelligently redirected loads to the least loaded phase, effectively reducing imbalances within three-phase lines. The integration of voltage control and stability ensured reliable operation even in fluctuating load scenarios.

Sutaya et al. [22] conducted studies on single-phase load balancing within three-phase sources. Their work addressed load balancing in consumers' power installations, demonstrating the effectiveness of their approach in achieving improved load distribution among single-phase loads on three-phase systems.

These studies have predominantly focused on single-phase load balancing, with our work extending the scope to tackle load balancing in three-phase systems. The distinction between single-phase and three-phase systems lies in their complexity, with three-phase systems demanding more advanced techniques for achieving balance.

3.2 Efficient Power Factor Correction Strategies

Coman et al. [23] presented a comprehensive analysis of the power factor's significance in network operations. They introduced equipment that enhanced the consumer power factor by integrating capacitors into power lines. Their novel power factor correction circuit, featuring remote configurability and telemetry, demonstrated reduced energy losses and improved operational efficiency through experimentation.

Rija et al. [24] developed an Arduino-based automated single-phase power factor correction system. Their system not only corrected power factor for various loads but also measured critical electrical parameters accurately. By connecting capacitors or inductors in parallel to the load, their system significantly improved power factor, ensuring efficient energy utilization.

Alam et al. [25] proposed a cost-effective method for power factor correction in single-phase domestic loads. Their continuous monitoring and correction system, implemented using Arduino, showcased the potential for substantial improvements in power factor and reduced current consumption.

Unlike previous research, which often focused on static power systems and single-phase loads, our approach introduces a real-time intelligent power factor correction system for dynamic and non-balanced three-phase loads. This novel approach

uses multi-step capacitors and inductors to dynamically correct power factor, considering the ever-changing nature of real-world power systems.

While individual studies have made notable contributions to dynamic load balancing and efficient power factor correction, there is a growing realization that a combined approach can offer a more holistic solution. The seamless interaction between load balancing and power factor correction promotes a harmonious power distribution environment. Such a configuration optimizes load distribution while simultaneously addressing reactive power imbalances. This integrated approach not only enhances energy utilization and power quality but also reduces system losses and supports sustainable energy practices.

In the rapidly evolving landscape of Industry 4.0, the challenge of maintaining high power quality and efficiency is increasingly prominent. With the advent of more dynamic and diverse power demands, traditional power management strategies often fall short, leading to significant energy wastage and operational inefficiencies. These challenges are further compounded by the need for real-time adaptability in power systems, which is critical for optimizing operational performance and sustainability in industrial settings. Addressing this gap, our paper presents a comprehensive implementation of dynamic load balancing and power factor correction techniques. This implementation aims to demonstrate not only the feasibility but also the significant benefits of these techniques in real-time scenarios. By integrating these advanced solutions into Industry 4.0 infrastructures, we seek to showcase a marked improvement in power quality and efficiency, setting a new benchmark for energy management in industrial applications. The objective is to provide a replicable and scalable model that can be adopted in various industrial contexts, ultimately contributing to more sustainable and efficient industrial practices.

4. PROPOSED METHODOLOGY

In our methodology, we adopt a Power Monitoring and Control Unit (PMCU) before each load in order to achieve our objectives. These PMCU units are connected to both the Main Control Unit (MCU) and the Main Power Monitoring Unit (MPMU), as shown in Figure 5. The primary goal of this architectural approach is to enable dynamic modifications to load wiring, which helps us attain an optimal load-balancing configuration. Additionally, our system has the capability to add or

remove capacitors or inductors before each load, thereby ensuring a power factor of 1.0 and further optimizing the load-balancing configuration. By incorporating advanced Industry 4.0 technologies, we enhance efficiency in terms of cost and time. A critical aspect of this architecture is the seamless communication between devices, which facilitates timely decision-making. To enable such capabilities, we have integrated IIOT-based devices into our system.

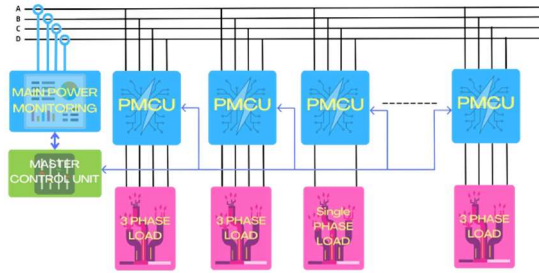


Figure 5: Schematic of the Proposed Automatic Three-Phase Load Balancing System.

Each PMCU is an Industrial Internet of Things (IIoT) device that combines various components (as depicted in Figure 6). It comprises a power monitoring unit capable of measuring voltage, current, power factor, active power, reactive power, and apparent power. Additionally, it incorporates a switching system that enables the reconfiguration of wiring across the three phases, facilitating the desired three-phase configuration. The PMCU also includes a power factor correction system, allowing for the adjustment of capacitors or inductances.

To oversee and regulate these functionalities, the PMCU incorporates a control unit that gathers data from both the monitoring unit and the main control unit. Utilizing the collected data, this control unit governs the switching system, implementing new wiring configurations when necessary. Furthermore, it possesses the ability to add or remove capacitors or inductors to attain the desired capacitance and inductance values.

The PMCU establishes communication with the main control unit, enabling coordination and information exchange between the devices. This communication ensures seamless integration within the system, facilitating effective control and monitoring of power-related parameters.

Overall, the PMCU functions as a comprehensive IIoT device that integrates power monitoring, switching, power factor correction, and control functionalities.

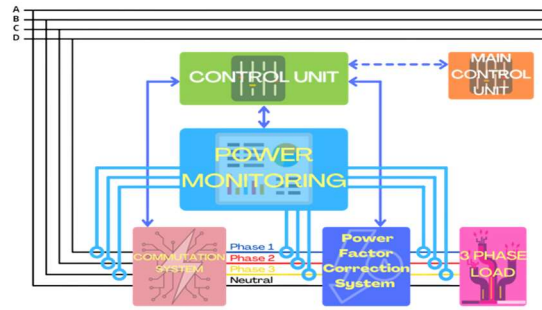


Figure 6: Schematic Diagram of Power Monitoring and Control Unit (PCMU) Components.

The system is structured to incorporate two main functionalities: the commutation system and the power factor correction system.

In the commutation system, each PMCU collects data from its Power Monitoring Unit (PMU). This data is sent to the main control unit periodically or when the PMCU is started. Since each load has its own PMCU, it operates independently from others. When a PMCU wants to connect a load to the power grid, it sends a request to the Main Control Unit (MCU). If the MCU has the history of that PMCU and the current data from the Main Power Monitoring Unit (MPMU) and other PMCUs, it sends the appropriate configuration. If there is no history available, the MCU sends out a random configuration until enough information is gathered to deliver the proper one. To find the best setting, the MCU occasionally broadcasts updated configurations to other PMCUs. The commutation system is used by the PMCU control unit to switch the phases. When it receives a configuration from the MCU, the switching may take some time if the load is still consuming energy. However, if the load can handle the interruption to its normal operation, the switching occurs immediately.

Similarly, in the power factor correction system, each PMCU periodically collects data from its own PMU. With each load having its own PMCU, they function independently, allowing for individual adjustment of capacitor and inductor configurations. When a PMCU intends to connect a load to the power grid or senses a change in power factor, it applies a configuration based on real-time data obtained from the PMU. As configuration changes do not affect load cycles, the new configuration is implemented and data is transmitted in real-time. This ensures that a new configuration is generated each time there is a change in power factor.

The power factor correction system is placed after the commutation system because it is dependent on the specific load requirements. In the upcoming power factor correction system section, we will delve into more detail about how the

correction is applied individually to each phase. Therefore, if the commutation system were to be positioned after the power factor correction system, any alterations made to the phase arrangement would require corresponding adjustments to the power factor correction configuration.

The commutation system requires the switching of four inputs, namely A, B, C, and D. To facilitate this, a 4-by-4 relay matrix (refer to Figure 7) is used. However, since the inputs represent a three-phase system, the neutral connection needs to be fixed only during the initiation of the PMCU (Power Management Control Unit). Only the three phases that require switching are involved, leading to the division of the commutation system into two blocks (refer to Figure 8). The first block encompasses the neutral detection and rerouting system, while the second block represents the newly optimized commutation system.

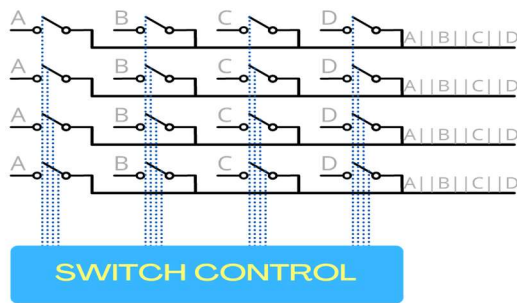


Figure 7: 4-by-4 Relay Matrix for Phase Switching.

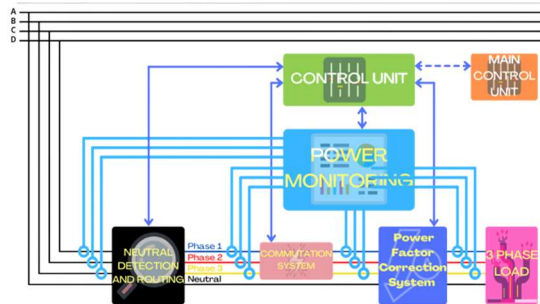


Figure 8: PMCU Components with Optimized Commutation and Neutral Rerouting.

In our design, the process of detecting and rerouting the neutral involves utilizing data collected by the PMU (Power Management Unit) and employing a combination of relays to direct the neutral to the appropriate output. Fortunately, out of the four wires in the system, three of them serve as phases, which means their order is not critical. Our objective is to ensure that only the neutral is routed correctly. To accomplish this, we utilize six relays, as depicted in Figure 9, with the specific configuration outlined in Table 2. The operating

principle of the relay (as illustrated in Figure 10) is that when it is in the "off" state, the output corresponds to input 1, whereas when it is in the "on" state, the output corresponds to input 2.

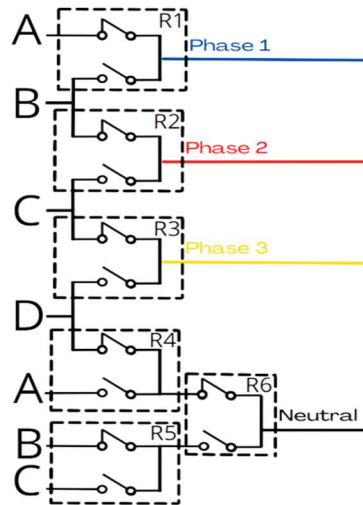


Figure 9: Schematic Diagram of the Neutral Detection and Routing System.

Table 2. Possible Configuration.

Neutral Input	Relay 1	Relay 2	Relay 3	Relay 4	Relay 5	Relay 6
A	On	On	On	On	X	Off
B	Off	On	On	X	Off	On
C	Off	Off	On	X	On	On
D	Off	Off	Off	Off	X	Off

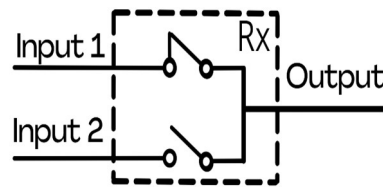


Figure 10. Schematic of a Relay.

As shown in Figure 11, a 3-by-3 relay matrix can represent the new commutation system. Since it is not possible for two phases to be directed to the same output, the various configurations of the commutation are described in Table 3.

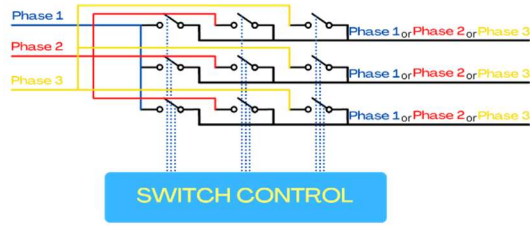


Figure 11. 3-by-3 Relay Matrix for New Commutation System.

Table 3. Possible Configurations of the New Commutation System.

Configuration	Output1	Output2	Output3
1	Pahse1	Pahse2	Pahse3
2	Pahse1	Pahse3	Pahse2
3	Pahse2	Pahse1	Pahse3
4	Pahse2	Pahse3	Pahse1
5	Pahse3	Pahse1	Pahse2
6	Pahse3	Pahse2	Pahse1

In order to determine the best configuration, we first need to establish a method for comparing two loads using a specific metric. For a three-phase load, it can be represented as a vector with three current components (I_1, I_2, I_3) . To compare these loads, we can simply compare the magnitudes of their respective vectors as described in (2). This magnitude value can be further developed as (3).

Next, we need to convert a configuration into a single load. This can be done by summing the currents of all the loads for each phase separately, as outlined in (4).

The optimal configuration is the one that results in the minimum magnitude, as determined by (5). If we incorporate (3), (4), and (5), we can derive (6). This process needs to be repeated for each possible case. Table 3 indicates that there are six possible configurations for one load. Therefore, the total number of possible configurations is 6^n , where n represents the number of loads.

$$I_{m,x} = \sqrt{I_{1,x}^2 + I_{2,x}^2 + I_{3,x}^2} \quad (2)$$

$$I_{m,x} = \sqrt{\sum_{i=1}^3 (I_{i,x})^2} \quad (3)$$

$$I_{i,x} = \sum_{j=0}^n I_{i,j} \quad (4)$$

$$OC = \min(I_{m,x}, I_{m,y}) \quad (5)$$

$$OC = \min \left(\sqrt{\sum_{i=1}^3 (\sum_{j=0}^n I_{i,j,x})^2}, \sqrt{\sum_{i=1}^3 (\sum_{j=0}^n I_{i,j,y})^2} \right) \quad (6)$$

The power factor correction system described earlier can be visualized as a three-phase system (Figure 12). This system comprises three individual blocks, each representing a single-phase power factor correction system (Figure 13). Each of these single-phase systems consists of a capacitor bank and an inductor bank (Figure 14).



Figure 12. Three-Phase Power Factor Correction System.

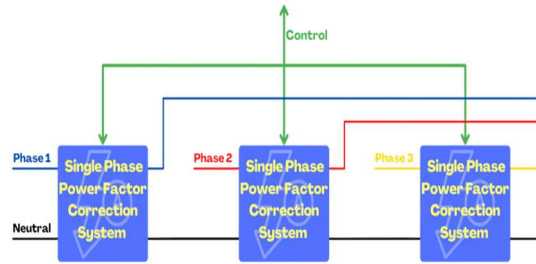


Figure 13. Internal Components of a Three-Phase Power Factor Correction System.

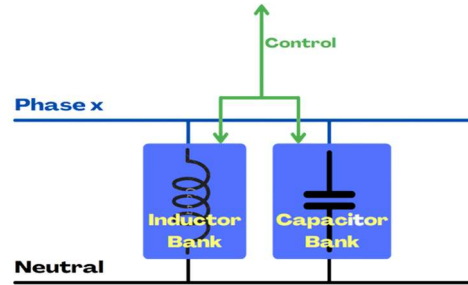


Figure 14. Internal Components of a Single-Phase Power Factor Correction System.

To achieve variable capacitance, we can utilize static capacitors connected in parallel, as their capacitance values add up when they are in parallel. These capacitors can be incorporated into the network using relays (Figure 15). This arrangement allows us to create a variable capacitor or variable capacitor bank, where the capacitance value of the bank, C_{Bank} , is determined as described in (7). In this equation, R_i represents the state of the relay (0 indicates the capacitor is not connected, while 1 indicates it is connected), and C_i represents the value of the respective capacitor.

$$C_{Bank} = \sum_{i=0}^n R_i * C_i \quad (7)$$

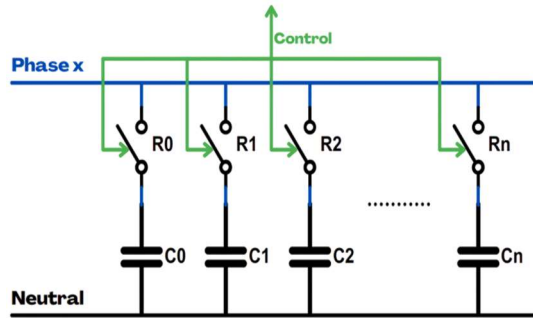


Figure 15. Capacitor Bank Diagram.

To achieve variable inductance, we can utilize static inductors connected in series, as their inductance values add up when they are in series. Furthermore, we can add relays in parallel with each inductor. By short-circuiting the relays, we can effectively cancel out the inductance and create a variable inductor or variable inductor bank (Figure 16). The value of the bank inductance, L_{Bank} , is determined as described in (8). In this equation, R_i represents the state of the relay (0 indicates the inductor is connected, while 1 means it is not connected or short-circuited), and L_i represents the value of the specific inductor. Additionally, we require a relay, RL , to disconnect the entire inductor bank when we want to have null inductance and prevent the phase with neutral from being short-circuited.

$$L_{Bank} = RL * (\sum_{i=0}^n (1 - R_i) * L_i) \quad (8)$$

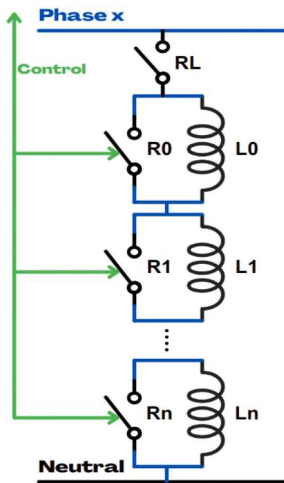


Figure 16. Inductor Bank Diagram.

The power factor is defined as the ratio of real power to apparent power (9). Real power refers to the power consumed by a load to perform useful work. In contrast, apparent power includes both real power and reactive power. Reactive power is required to maintain the magnetic or electric fields

in the load but does not contribute to performing useful work.

Real power can be calculated by multiplying the voltage and current with the cosine of the phase angle between them (10). On the other hand, apparent power can be obtained either by taking the vector sum of real power and reactive power (11) or by multiplying the voltage and current directly (12).

From (10) and (12), it can be concluded that the power factor is the cosine of the phase angle between the current and voltage (13), which can vary from -1.0 to 1.0. A power factor of 1.0 indicates an ideal system with no reactive components, where the apparent power and real power are equivalent.

Our objective is to design a system that consistently maintains a power factor of 1.0, meaning that the reactive power is effectively eliminated. This ensures that the power used by the load is purely for performing useful work, and there is no power returned to the power source due to reactive elements in the circuit.

$$PF = \frac{Real\ Power\ P}{Apparent\ Power} = \frac{P}{S} \quad (9)$$

$$P = V * I * \cos(\varphi) \quad (10)$$

$$S = \sqrt{P^2 + Q^2} \quad (11)$$

$$S = V * I \quad (12)$$

$$PF = \frac{V * I * \cos(\varphi)}{V * I} = \cos(\varphi) \quad (13)$$

We can utilize an MPU (Measurement Processing Unit) to measure the reactive power and then employ inductors or capacitors to counteract it and achieve a reactive power of zero. Reactive power can be either leading or lagging. When the load is capacitive, it can store energy in an electric field and release it back into the circuit, resulting in leading reactive power (14). In this case, the current leads the voltage, and the phase angle between them is negative. Conversely, when the load is inductive, it can store energy in a magnetic field and release it back into the circuit, resulting in lagging reactive power (15). Here, the current lags behind the voltage, and the phase angle between them is positive.

In simple terms, if the reactive power is negative, it indicates a capacitive load, and we need to add inductance to the system to correct it. On the other hand, if the reactive power is positive, it implies an inductive load, and we need to add capacitors.

Once we have measured the reactive power, we need to determine the necessary capacitance or inductance to rectify it. To achieve a total reactive power of zero, we must apply reactive power that has the opposite sign of the load's power factor (16). This can also be expressed as a function of real power and the power factor (17). Utilizing (14) and (17), we can calculate the required capacitance as described in (18). Similarly, using (15) and (17), we can determine the necessary inductance as shown in (19).

$$Q_{capacitor} = -C\omega V^2 \tag{14}$$

$$Q_{inductor} = \frac{V^2}{L\omega} \tag{15}$$

$$Q_{applied} = -Q_{load} \tag{16}$$

$$Q_{applied} = -P_{load} \tan(\cos^{-1}(PF_{load})) \tag{17}$$

$$C = \frac{P_{load} \tan(\cos^{-1}(PF_{load}))}{\omega * V^2} \tag{18}$$

$$L = -\frac{V^2}{\omega * P_{load} \tan(\cos^{-1}(PF_{load}))} \tag{19}$$

To determine the minimum and maximum required capacitance and inductance, we generated Table 4 for capacitance using (18) and Table 5 for inductance using (19). These tables were created considering a range of real power from 100W to 1MW, a power factor range of 0.01 to 0.99 for the capacitor case, and a power factor range of -0.99 to -0.01 for the inductor case. The results obtained from the tables indicate that the minimum required capacitance is approximately 1µF, and the maximum required capacitance is around 6.6F. Similarly, the minimum required inductance is around 1.5µH, while the maximum required inductance is approximately 10.8H.

Table 4. Capacitance Requirements Based on Real Power and Power Factor.

P(W)/PF	0.01	0.1	0.5	0.9	0.99
100	657.63	65.44	11.39	3.19	0.94
1000	6576.32	654.37	113.91	31.85	9.37
10000	65763.2 2	6543.68	1139.11	318.52	93.71
100000	657632. 17	65436.8 5	11391.0 9	3185.22	937.12
1000000	6576321 .70	654368. 47	113910. 93	31852.1 7	9371.22

Table 5. Inductance Requirements Based on Real Power and Power Factor.

P(W)/PF	-0.99	-0.9	-0.5	-0.1	-0.01
100	1081195 2.91	3180981 .90	889477. 28	154838. 12	15406.9 7
1000	1081195 .29	318098. 19	88947.7 3	15483.8 1	1540.70
10000	108119. 53	31809.8 2	8894.77	1548.38	154.07
100000	10811.9 5	3180.98	889.48	154.84	15.41
1000000	1081.20	318.10	88.95	15.48	1.54

The tables were generated to demonstrate how capacitance and inductance vary in relation to changes in real power and power factor. If our goal was solely to calculate the minimum and maximum values, we could have directly used (20), (21), (22), and (23).

$$C_{min} = \frac{P_{load,min} \tan(\cos^{-1}(PF_{load,max}))}{\omega * V^2} \tag{20}$$

$$C_{max} = \frac{P_{load,max} \tan(\cos^{-1}(PF_{load,min}))}{\omega * V^2} \tag{21}$$

$$L_{min} = -\frac{V^2}{\omega * P_{load,max} \tan(\cos^{-1}(PF_{load,max}))} \tag{22}$$

$$L_{max} = -\frac{V^2}{\omega * P_{load,min} \tan(\cos^{-1}(PF_{load,min}))} \tag{23}$$

In order to achieve the desired capacitance or inductance values within their respective ranges, it is necessary to consider the minimum value of the component as the base. However, this theoretical approach is not feasible in practical situations. For example, if we wanted to achieve a capacitance of 6.6F using a base value of 1µF, we would need to connect 6.6 million capacitors in parallel. Similarly, if we aimed to achieve an inductance of 10.8H using a base value of 1.5µH, we would require a series connection of 7.2 million inductors. To optimize the design, capacitor banks, and inductor banks employ relays that have binary states, either 0 or 1. We can treat each relay as a binary bit, and instead of duplicating a single component value, we can multiply the minimum value by 2 raised to the power of n. This approach is illustrated in (24) and (25), where C_i and L_i represent the desired capacitance and inductance, respectively, and "i" denotes the bit index.

$$C_i = C_{min} * 2^i \tag{24}$$

$$L_i = L_{min} * 2^i \quad (25)$$

We can determine the number of capacitors, N_C , needed when (24) reaches its maximum capacity, as illustrated in (26). Similarly, we can calculate the number of inductors, N_L , required when (25) reaches the maximum inductance, as shown in (27). These equations can be further developed into (28) and (29) respectively. By applying a logarithmic transformation, we obtain (30) and (31 respectively). Utilizing (20), (21), and (30), we can derive (32). Similarly, by employing (22), (23), and (31), we can derive (33). As N_C and N_L represent real components, we may need to round up their results if necessary.

$$C_{N_C} = C_{max} \quad (26)$$

$$L_{N_L} = L_{max} \quad (27)$$

$$C_{min} * 2^{N_C} = C_{max} \quad (28)$$

$$L_{min} * 2^{N_L} = L_{max} \quad (29)$$

$$N_C = \log_2 \left(\frac{C_{max}}{C_{min}} \right) \quad (30)$$

$$N_L = \log_2 \left(\frac{L_{max}}{L_{min}} \right) \quad (31)$$

$$N_C = \log_2 \left(\frac{P_{load,max} \tan(\cos^{-1}(PF_{load,min}))}{P_{load,min} \tan(\cos^{-1}(PF_{load,max}))} \right) \quad (32)$$

$$N_L = \log_2 \left(\frac{P_{load,max} \tan(\cos^{-1}(PF_{load,max}))}{P_{load,min} \tan(\cos^{-1}(PF_{load,min}))} \right) \quad (33)$$

In our case, the number of capacitors (N_C) and inductors (N_L) is both equal to 23 components. The capacitance range extends from 0 to $C_{min} * (2^{23} - 1) = 7.86F$ with a step size of C_{min} . Similarly, the inductance range spans from 0 to $L_{min} * (2^{23} - 1) = 12.92H$ with a step size of L_{min} .

To determine the appropriate capacitors or inductors needed to achieve a desired capacitance value for the capacitor bank (C_{Bank}) or an inductance value for the inductor bank (L_{Bank}), we can utilize (7), (18), and (24) to derive (34) for the capacitors. Similarly, (8), (19), and (25) can be used to obtain (35) for the inductors (assuming RL is set to 1 for the desired inductance value). These equations can be further simplified into (36) and (37), which involve a straightforward conversion from decimal to binary as shown in(38). The outputs of (36) and (37) are real

numbers, so rounding is necessary before applying the decimal-to-binary conversion. In the capacitor equation, the binary state b_i corresponds to the relay state R_i , while in the inductor equation, the binary state b_i is the complement of the relay state R_i .

$$\sum_{i=0}^{N_C} R_i * C_{min} * 2^i = \frac{P_{load} \tan(\cos^{-1}(PF_{load}))}{\omega * V^2} \quad (34)$$

$$\sum_{i=0}^{N_L} (1 - R_i) * L_{min} * 2^i = -\frac{V^2}{\omega * P_{load} \tan(\cos^{-1}(PF_{load}))} \quad (35)$$

$$\sum_{i=0}^{N_C} R_i * 2^i = \frac{P_{load} \tan(\cos^{-1}(PF_{load}))}{C_{min} * \omega * V^2} \quad (36)$$

$$\sum_{i=0}^{N_L} \underline{R}_i * 2^i = -\frac{V^2}{L_{min} * \omega * P_{load} \tan(\cos^{-1}(PF_{load}))} \quad (37)$$

$$b_0 * 2^0 + b_1 * 2^1 + \dots + b_n * 2^n = Decimal \quad (38)$$

5. RESULTS AND DISCUSSION

An evaluation was conducted at a plant, where ten machines were randomly selected for assessment. Each machine consisted of various components such as induction heating systems, motors, vibrators, heating resistors, casting machines, molding machines, and more. The data were collected multiple times at random intervals. The collected data for the first sample of one of the ten machines, referred to as devices, is presented in Table 6. The table includes a range of electrical parameters related to the load. These parameters include voltages V1, V2, and V3 between each phase and neutral, currents I1, I2, and I3 for each phase, power factors PF1, PF2, PF3, and Pft (total power factor of the load), frequency F, real powers P1, P2, P3, and Pt (total real power of the load), reactive powers Q1, Q2, Q3, and Qt (total reactive power of the load), and apparent powers S1, S2, S3, and St (total apparent power of the load). These parameters specifically pertain to the load itself. The evaluation comprised three tests: the first test focused solely on the commutation system, the second test examined the power factor correction system alone, and the third test evaluated the combined solution of both systems.

Table 6. Collected Data on Electrical Parameters and Load Characteristics from Ten Devices.

Name	Device 1	Device 2	Device 3	Device 4	Device 5	Device 6	Device 7	Device 8	Device 9	Device 10
V1	222.20	221.87	222.39	222.88	220.51	221.85	220.65	221.61	220.79	222.52
V2	221.85	220.35	222.92	220.85	220.01	221.66	221.77	222.66	220.42	220.07
V3	222.57	222.56	221.08	221.88	221.69	220.56	220.43	222.59	222.14	221.11
I1	235.42	214.43	287.15	129.82	109.98	147.29	143.77	29.64	218.32	147.57
I2	154.78	170.18	270.98	179.32	121.49	55.25	295.31	235.12	110.47	31.89
I3	270.07	258.37	169.92	176.40	230.38	88.30	117.93	254.09	185.59	82.98
PF1	0.75	0.62	0.75	0.63	0.64	0.74	0.75	0.80	0.67	0.66
PF2	0.68	0.76	0.77	0.75	0.64	0.75	0.63	0.71	0.74	0.67
PF3	0.78	0.75	0.68	0.72	0.71	0.63	0.62	0.76	0.79	0.63
PFt	0.74	0.71	0.74	0.71	0.68	0.71	0.66	0.74	0.73	0.65
F	50.59	50.81	50.36	50.40	50.62	50.90	50.63	50.94	50.58	50.06
P1	39111.40	29356.95	47635.29	18126.96	15443.91	24141.07	23840.32	5248.18	32106.67	21680.73
P2	23298.67	28678.73	46625.20	29523.58	17094.50	9140.48	41410.73	37230.43	17931.34	4675.36
P3	46708.93	42991.45	25701.89	28328.24	36426.65	12348.35	16133.38	43024.63	32457.75	11525.66
Pt	109119.00	101027.13	119962.38	75978.77	68965.07	45629.90	81384.43	85503.24	82495.76	37881.75
Q1	34735.15	37436.34	42533.57	22551.71	18698.69	22021.29	20928.95	3951.11	35953.12	24664.83
Q2	25225.76	24161.38	38408.05	26396.74	20549.19	8149.81	50739.85	36805.74	16474.87	5235.39
Q3	37832.45	38188.51	27396.19	27007.18	35798.48	15059.54	20383.48	36710.75	25417.13	14273.92
Qt	97793.36	99786.23	108337.80	75955.63	75046.36	45230.65	92052.28	77467.60	77845.12	44174.14
S1	52309.01	47574.26	63860.99	28933.83	24251.92	32676.12	31723.52	6569.22	48202.33	32839.12
S2	34339.00	37499.89	60407.67	39603.40	26729.97	12246.13	65493.37	52352.34	24350.65	7019.14
S3	60108.39	57503.27	37565.12	39139.20	51072.81	19474.89	25995.62	56557.91	41225.43	18346.27
St	146528.15	141999.20	161641.74	107433.85	101922.21	64248.73	122870.05	115377.78	113425.80	58192.62

In the first test, which focuses on the commutation system, the objective is to determine the optimal configuration. However, it is also valuable to explore the worst configuration in order to compare all three cases: the original configuration, the optimal configuration, and the worst configuration. The worst configuration refers to the one that yields the maximum magnitude, as specified by (39). By incorporating (3), (4), and (39), we can derive (40). To establish a metric for comparing the original, optimal, and worst configurations, we can utilize the Unbalance percentage. This metric can be calculated using the Root Mean Square (RMS) of the deviations, also known as the RMS unbalance factor (41), and the average current (42). (43) provides the Unbalance percentage. Furthermore, (43) can be further developed into (44).

$$WC = \max(I_{m,x}, I_{m,y}) \tag{39}$$

$$WC = \max\left(\sqrt{\sum_{i=1}^3 (\sum_{j=0}^n I_{i,j,x})^2}, \sqrt{\sum_{i=1}^3 (\sum_{j=0}^n I_{i,j,y})^2}\right) \tag{40}$$

$$I_{RMSD} = \sqrt{\sum_{i=1}^3 (I_{i,x} - I_{avg,x})^2} \tag{41}$$

$$I_{avg,x} = \frac{\sum_{i=1}^3 I_{i,x}}{3} \tag{42}$$

$$Unbalance = \frac{I_{RMSD}}{I_{avg,x}} * 100\% \tag{43}$$

$$Unbalance = \frac{\sqrt{\sum_{i=1}^3 (I_{i,x} - I_{avg,x})^2}}{I_{avg,x}} * 100\% \tag{44}$$

In Table 7, we can observe the collected data for the first sample. The table focuses solely on the current data since the commutation system utilizes only the current information. This data is represented as the original configuration. Furthermore, the table includes the optimal and worst configurations, along with the corresponding "Cfg" column indicating the configuration used (to see the corresponding configuration found in the Cfg column, refer to Table 3). The table also provides the magnitude of each configuration, including the "IRMSD" (Root Mean Square Deviation of Current), the "Iavg" (Average Current), and the "Unbalanced percentage." Upon analyzing the data, it is evident that the worst configuration exhibits the highest unbalanced percentage, which amounts to 89.98 percent. In contrast, the original configuration, which represents the pre-wired state of the devices, demonstrates an unbalanced percentage of 36.88 percent. Notably, the optimal configuration shows no unbalance.

Table 7. Comparative Analysis of Original, Worst, and Optimal Configurations.

Name	Original				Optimal				Worst			
	I1	I2	I3	Cfg	I1	I2	I3	Cfg	I1	I2	I3	Cfg
Device 1	235.42	154.78	270.07	0	235.42	154.78	270.07	0	235.42	154.78	270.07	0
Device 2	214.43	170.18	258.37	0	258.37	170.18	214.43	5	214.43	170.18	258.37	0
Device 3	287.15	270.98	169.92	0	287.15	270.98	169.92	0	270.98	169.92	287.15	3
Device 4	129.82	179.32	176.40	0	176.40	179.32	129.82	5	176.40	129.82	179.32	4
Device 5	109.98	121.49	230.38	0	230.38	109.98	121.49	4	121.49	109.98	230.38	2
Device 6	147.29	55.25	88.30	0	88.30	55.25	147.29	5	88.30	55.25	147.29	5
Device 7	143.77	295.31	117.93	0	143.77	295.31	117.93	0	143.77	117.93	295.31	1
Device 8	29.64	235.12	254.09	0	29.64	254.09	235.12	1	235.12	29.64	254.09	2
Device 9	218.32	110.47	185.59	0	110.47	185.59	218.32	3	185.59	110.47	218.32	5
Device 10	147.57	31.89	82.98	0	147.57	31.89	82.98	0	82.98	31.89	147.57	5
Sum	1663.39	1624.81	1834.01		1707.47	1707.38	1707.36		1754.47	1079.87	2287.88	
Mod	2961.50				2957.31				3078.74			
Avg	1707.41				1707.41				1707.41			
Mod Avg	157.44				0.08				856.13			
Unbalance	9.22				0.00				50.14			

In Table 7, we initially examined data from a single sample. However, to provide a more comprehensive analysis, we randomly selected 30 samples from our pre-collected dataset. For each of these samples, we recorded unbalanced values across the original, optimal, and worst configurations. Subsequently, we calculated the average unbalance across these thirty samples and presented the findings in Figure 17.

Upon scrutinizing the data, it becomes evident that our approach demonstrates remarkable potential in achieving a nearly perfectly balanced system. Specifically, the optimal configuration boasts an average unbalance of only 0.07 percent, with minimum and maximum values of 0.01 percent and 0.017 percent, respectively. These results signify a system that is exceptionally well-balanced.

Conversely, the original configuration exhibits an average unbalance of approximately 19.895 percent, with a range spanning from 2.744 percent to 72.016 percent. This starkly contrasts with the optimal configuration, highlighting the significant unbalance present in the original setup.

In the worst-case scenario, the average unbalance reaches approximately 61.196 percent, with minimum and maximum values of 37.723 percent and 78.876 percent. These results underscore the substantial level of unbalance inherent in the worst configuration.

In summary, our data and visual representation clearly demonstrate the effectiveness of our approach in achieving a high degree of balance within the system. The optimal configuration stands out for its minimal unbalance, offering a marked improvement over both the original and worst configurations.

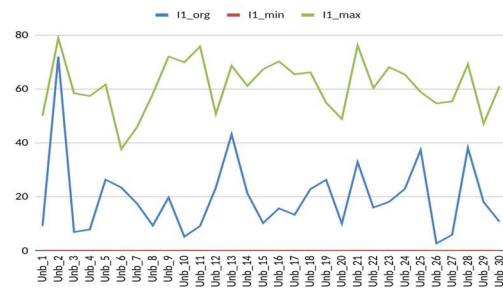


Figure 17: Comparing Balancing Performance in Optimal, Original, and Worst Configurations.

For the second test, which focuses on the power factor correction system, we conducted an initial analysis of the plant. During this analysis, we found that capacitive loads were not present, which is typically the case in the industry as capacitive loads are rarely encountered. Therefore, the results presented here are based on inductive loads. However, it's important to note that if capacitive loads were encountered, the same results would be obtained.

One of the key parameters we determined during the analysis was the minimum and maximum power per phase. We found that the minimum power per phase ($P_{load,min}$) was 132W, while the maximum power per phase ($P_{load,max}$) was 66231W. Using these parameters, we calculated the minimum capacitance needed (C_{min}) as 1 μ F and the maximum capacitance needed (C_{max}) as 5808 μ F.

Based on these calculations, we determined that 13 capacitors would be required for the power factor correction system (i.e., NC=13). This number of capacitors is necessary to achieve the desired power factor correction based on the given load

parameters. However, it is worth noting that the system can accommodate a capacitance of up to 8,191µF if needed.

In a manner akin to our initial test, Table 8 presents the data collected from the first sample. This table provides the necessary capacitance values for each phase (C1, C2, and C3), aiming to improve the power factor. These values are derived from the data presented in Table 6. Furthermore, the table displays the status of the relay configuration (R1, R2, and R3) required to achieve the desired capacity,

along with the resulting achieved capacity (NC1, NC2, and NC3). Additionally, the table includes the corresponding reactive powers (QC1, QC2, QC3, and QCt), collectively representing the total reactive power of the capacitors.

Following the implementation of the capacitor configuration, Table 9 presents the updated data. This dataset encompasses the newly acquired values of reactive power, denoted as NQ1, NQ2, NQ3, and NQt, resulting from the integration of capacitors with the load. Furthermore, the apparent

Table 8. Capacitance and Relay Settings for Improved Power Factor.

Name	Device 1	Device 2	Device 3	Device 4	Device 5	Device 6	Device 7	Device 8	Device 9	Device 10
C1	2213.10	2382.28	2717.81	1433.62	1209.22	1399.06	1351.37	251.34	2320.80	1583.76
C2	1612.28	1558.71	2442.54	1708.99	1334.89	518.67	3243.18	2319.31	1067.08	343.70
C3	2402.51	2414.97	1771.43	1732.36	2290.36	967.98	1318.80	2314.79	1620.89	928.35
R1	01000101 00101	01001010 01110	01010100 11110	00101100 11010	00100101 11001	00101011 10111	00101010 00111	00000111 11011	01001000 10001	00100001 10000
R2	00110010 01100	00110000 10111	01001100 01011	00110101 01101	00101001 10111	00010000 00111	01100101 01011	01001000 01111	00100001 01011	00001010 11000
R3	01001011 00011	01001011 01111	00110111 01011	00110110 00100	01000111 10010	00011110 01000	00101001 00111	01001000 01011	00110010 10101	00011101 00000
NC1	2213	2382	2718	1434	1209	1399	1351	251	2321	1584
NC2	1612	1559	2443	1709	1335	519	3243	2319	1067	344
NC3	2403	2415	1771	1732	2290	968	1319	2315	1621	928
QC1	-34733.55	-37432.00	-42536.59	-22557.62	-18695.26	-22020.37	-20923.26	-3945.77	-35956.28	-24668.50
QC2	-25221.36	-24165.90	-38415.30	-26396.91	-20550.90	-8154.98	-50737.09	-36800.75	-16473.70	-5239.88
QC3	-37840.17	-38188.94	-27389.57	-27001.53	-35792.84	-15059.80	-20386.64	-36714.01	-25418.79	-14268.51
QCt	-97795.08	-99786.83	-108341.5	-75956.06	-75039.00	-45235.16	-92046.99	-77460.53	-77848.77	-44176.89

Table 9. Reactive Power, Apparent Power, and Power Factor Data Post Capacitor Integration.

Name	Device 1	Device 2	Device 3	Device 4	Device 5	Device 6	Device 7	Device 8	Device 9	Device 10
NQ1	1.6018	4.3430	-3.0186	-5.9135	3.4318	0.9221	5.6959	5.3348	-3.1558	-3.6773
NQ2	4.3963	-4.5162	-7.2504	-0.1692	-1.7079	-5.1710	2.7574	4.9888	1.1695	-4.4974
NQ3	-7.7149	-0.4302	6.6112	5.6524	5.6386	-0.2643	-3.1622	-3.2569	-1.6614	5.4173
NQt	-1.7169	-0.6034	-3.6577	-0.4302	7.3625	-4.5132	5.2911	7.0666	-3.6477	-2.7574
AC1	99.9954	99.9884	99.9929	99.9738	99.9817	99.9958	99.9728	99.8652	99.9912	99.9851
AC2	99.9826	99.9813	99.9811	99.9994	99.9917	99.9366	99.9946	99.9864	99.9929	99.9142
AC3	99.9796	99.9989	99.9759	99.9791	99.9843	99.9982	99.9845	99.9911	99.9935	99.9621
ACt	99.9982	99.9994	99.9966	99.9994	99.9902	99.9900	99.9943	99.9909	99.9953	99.9938
NS1	39111.40	29356.95	47635.29	18126.96	15443.91	24141.07	23840.32	5248.18	32106.67	21680.73
NS2	23298.67	28678.73	46625.20	29523.58	17094.50	9140.48	41410.73	37230.44	17931.34	4675.37
NS3	46708.93	42991.45	25701.89	28328.24	36426.65	12348.35	16133.38	43024.63	32457.75	11525.66
NSt	109119.00	101027.13	119962.38	75978.77	68965.07	45629.90	81384.43	85503.24	82495.76	37881.75
NPF1	1.00	1.00	1.00	1.00	1.00	1.00	1.00	1.00	1.00	1.00
NPF2	1.00	1.00	1.00	1.00	1.00	1.00	1.00	1.00	1.00	1.00
NPF3	1.00	1.00	1.00	1.00	1.00	1.00	1.00	1.00	1.00	1.00
NPFt	1.00	1.00	1.00	1.00	1.00	1.00	1.00	1.00	1.00	1.00
NI1	176.02	132.32	214.19	81.33	70.04	108.82	108.04	23.68	145.42	97.43
NI2	105.02	130.15	209.15	133.68	77.70	41.24	186.72	167.21	81.35	21.24
NI3	209.87	193.16	116.26	127.67	164.31	55.99	73.19	193.29	146.12	52.13
PI1	44.09	61.92	44.36	60.75	59.45	45.42	43.52	36.18	55.63	56.41
PI2	53.97	41.51	40.43	44.43	59.10	44.29	60.02	49.43	45.77	55.63
PI3	39.61	44.10	53.19	47.61	49.13	59.80	61.48	42.13	38.01	60.53
PIt	43.50	49.36	44.18	49.10	52.53	48.76	57.39	45.43	47.92	57.34
Pr1	25.23	38.29	25.41	37.35	36.32	26.12	24.85	20.11	33.39	33.98
Pr2	32.15	23.52	22.82	25.45	36.05	25.36	36.77	28.88	26.36	33.39
Pr3	22.29	25.24	31.58	27.62	28.68	36.59	37.94	23.93	21.27	37.18
Prt	25.53	28.85	25.79	29.28	32.34	28.98	33.76	25.89	27.27	34.90

power values after the capacitor integration are indicated as NS1, NS2, NS3, and NSt. The revised power factors are represented by NPF1, NPF2, NPF3, and NPFt. Additionally, the refreshed values of current consumption are specified as NI1, NI2, and NI3.

In our quest for a suitable accuracy metric (PFCP1, PFCP2, PFCP3, and PFCPt), our initial approach revolved around the use of (45). This equation, designed to quantify accuracy as a percentage based on deviations from the desired power factor, initially showed promise but revealed limitations in comprehensively capturing the intricacies of our power factor correction process.

Given the unique nature of our system, which involves manipulating reactive power to impact the power factor, the need for a more appropriate assessment metric became evident. This prompted the introduction of an alternative metric (AC1, AC2, AC3, and ACt) denoted as (46), offering distinct advantages. (46) takes into account both the initial reactive power state and the absolute magnitude of reactive power change resulting from intentional adjustments. This formulation aligns closely with the physical components, including capacitors and inductors, involved in these transformations.

The strength of (46) lies in its ability to precisely quantify the efficacy of power factor adjustments while concurrently considering essential modifications in reactive power. This equation seamlessly harmonizes intricate dynamics, resulting in a more nuanced and insightful appraisal of system performance. By evaluating the proficiency of our system in managing the interaction between power factor adjustments and changes in reactive power, (46) provides a comprehensive measure of power factor correction accuracy that intimately reflects the real-world dynamics of our system. Additionally, to calculate the cumulative accuracy across devices for a specific time, we employed (47), derived from (46), with "n" representing the number of devices.

Going beyond accuracy, we can assess the effectiveness of our solution by examining power loss reduction and power consumption reduction metrics. The percentages of power loss reduction (Pl1, Pl2, and Pl3) were determined using (48), which can be expanded into (49) and (50). The overall power loss reduction (Plt) was computed using (51), derived from (48). Additionally, to calculate the cumulative reduction in power loss across all devices over a specific time, we applied (53), derived from (52), with "n" representing the number of devices. Similarly, the percentages of

power usage reduction (Pr1, Pr2, and Pr3) were calculated using (54). The overall power usage reduction (Prt) was determined using (55), with the total apparent power determined by (56). For the calculation of the cumulative reduction in power usage across all devices for a specific time, we utilized (55), with the total apparent power determined by (57), and "n" representing the number of devices. These calculations provide valuable insights into the improvements achieved in terms of power loss and usage through the implementation of power factor correction measures.

$$PFCP_{(1,2,3,t)} = \left(1 - \left| \frac{NPFx-}{1} \right| \right) * 100\% \quad (45)$$

$$AC_{(1,2,3,t)} = \frac{Q_{(1,2,3,t)}}{Q_{(1,2,3,t)} + |NQ_{(1,2,3,t)}|} * 100\% \quad (46)$$

$$totAC = \frac{\sum_{i=0}^n Q_{t,i}}{Q_{t,i} - \sum_{i=0}^n NQ_{t,i}} * 100\% \quad (47)$$

$$Pl_{(1,2,3)} = \frac{P_{j(1,2,3),old} - P_{j(1,2,3),new}}{P_{j(1,2,3),old}} * 100\% \quad (48)$$

$$Pl_{(1,2,3)} = \frac{R_{(1,2,3)} * I_{(1,2,3),old}^2 - R_{(1,2,3)} * I_{(1,2,3),new}^2}{R_{(1,2,3)} * I_{(1,2,3),old}^2} * 100\% \quad (49)$$

$$Pl_{(1,2,3)} = \frac{I_{(1,2,3),old}^2 - I_{(1,2,3),new}^2}{I_{(1,2,3),old}^2} * 100\% \quad (50)$$

$$Plt = \frac{\sum_{i=0}^3 P_{j,i,old} - \sum_{i=0}^3 P_{j,i,new}}{\sum_{i=0}^3 P_{j,i,old}} * 100\% \quad (51)$$

$$Plt = \frac{\sum_{i=0}^3 I_{i,old}^2 - \sum_{i=0}^3 I_{i,new}^2}{\sum_{i=0}^3 I_{i,old}^2} * 100\% \quad (52)$$

$$totPlt = \frac{\sum_{i=0}^n (\sum_{j=0}^3 I_{j,old}^2) - \sum_{i=0}^n (\sum_{j=0}^3 I_{j,new}^2)}{\sum_{i=0}^n (\sum_{j=0}^3 I_{j,old}^2)} * 100\% \quad (53)$$

$$Pr_{(1,2,3)} = \frac{S_{(1,2,3),old} - S_{(1,2,3),new}}{S_{(1,2,3),old}} * 100\% \quad (54)$$

$$Prt = \frac{St_{old} - St_{new}}{St_{old}} * 100\% \quad (55)$$

$$St_{(old,new)} = \sqrt{Pt_{(old,new)}^2 + Qt_{(old,new)}^2} \quad (56)$$

$$\sqrt{\frac{St_{(old,new)}}{(\sum_{i=0}^n Pt_{i,(old,new)})^2 + (\sum_{i=0}^n Qt_{i,(old,new)})^2}} \quad (57)$$

In addition to the data shown in Tables 6, 8, and 9, which encompass information gathered from the initial set of ten devices, our research extends to cover successive phases of data collection. This

ongoing process generates new datasets structured similarly to Tables 6, 8, and 9. As time advances, each new dataset offers deeper insights into the behavior of the devices under varying conditions.

Upon meticulous examination of the data in Tables 6, 8, and 9, alongside their counterparts from subsequent collection phases, several significant observations emerge regarding the inherent non-linearity of the loads. Each individual phase exhibits its own distinct current and power factor values ($PF_1 \neq PF_2 \neq PF_3$). Moreover, the non-linear characteristics of the loads display fluctuations over time ($PF_{1,t0} \neq PF_{1,t1} \neq PF_{1,t2} \dots; PF_{2,t0} \neq PF_{2,t1} \neq PF_{2,t2} \dots; PF_{3,t0} \neq PF_{3,t1} \neq PF_{3,t2} \dots$). This underscores the necessity of considering adaptable capacitance solutions tailored to the complexities of the system. Even when considering variable capacitance solutions, maintaining independent control over the capacitance of each phase remains crucial.

Given the substantial power consumption and the dynamic nature of load behavior, it is advisable to strategically distribute the capacitor banks across each individual load. This allocation strategy helps minimize the need for frequent relay switching due to load variations. Additionally, it is essential to note that deploying a substantial capacitor bank could lead to increased current demand and the generation of harmonics, phenomena particularly relevant in this context.

The implementation of power factor correction yields significant improvements in power factor within this system, with most values converging toward the desired optimal value of 1.0. This corrective measure not only reduces apparent power, resulting in tangible cost savings, but also diminishes current draw, subsequently reducing power loss. Furthermore, the resulting capacitance values after implementing these corrections closely align with the intended capacitance levels.

It is important to highlight that the degree of deviation from the power factor of 1.0 corresponds to the potential for reducing power consumption and mitigating power loss within the system. Consequently, lower power factor values indicate a greater potential for achieving these favorable outcomes.

To showcase the effectiveness of our approach, similar to the first test, we randomly selected 30 samples from the pre-collected data. Figure 18 illustrates the accuracy of our method across various time intervals for each device. ACt_1 through ACt_30 represent the overall accuracy of specific devices at specific time points. This figure clearly demonstrates our method's consistent

achievement of accuracy exceeding 99.931% for any device within the given time frame.

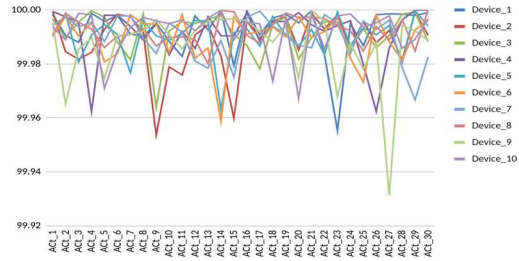


Figure 18. Accuracy Trends Over Time for Individual Devices.

Now turning to Figure 19, we depict the cumulative accuracy across devices for specific time intervals. Remarkably, our method consistently achieves a total accuracy surpassing 99.992% at each time step.

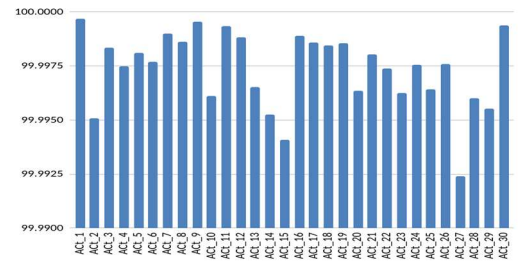


Figure 19. Cumulative Accuracy Across Devices Over Time.

Figure 20 captures the power loss reduction achieved by our approach for individual devices across different time intervals. Plt_1 through Plt_30 indicate the total power loss reduction percentage for specific devices at specified times. It is evident that our method consistently accomplishes power loss reduction exceeding 36.88% for any device within the specified time period.

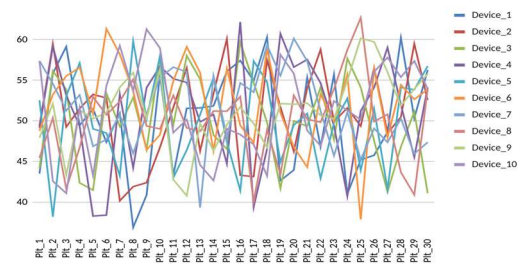


Figure 20. Power Loss Reduction Trends Across Devices Over Time.

In Figure 21, we illustrate the cumulative power loss reduction across devices for a specific

time. Impressively, our method maintains a significant overall reduction in power loss, surpassing 49.097% at every time step.

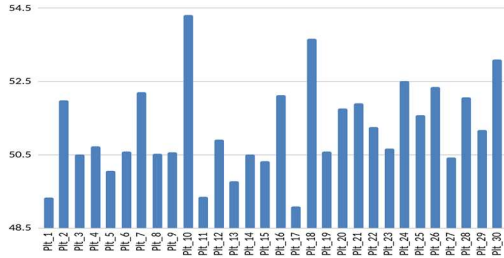


Figure 21. Cumulative Power Loss Reduction Across Devices Over Time.

Figure 22 delves into the trends of power usage reduction for different devices and time intervals. Prt_1 through Prt_20 represent the total power usage reduction percentages for specific devices during designated time periods. Here, we observe our method's consistent achievement of power usage reduction surpassing 20.769% for any device at a given time.

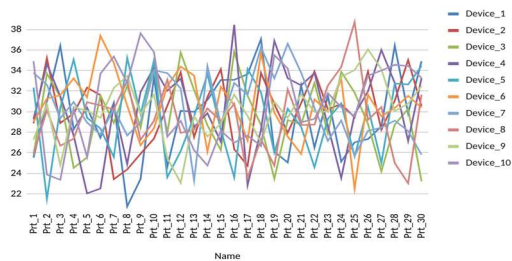


Figure 22. Power Usage Reduction Trends for Different Devices and Time Intervals.

Similarly, Figure 23 presents the cumulative power usage reduction across devices for a specific time. The data reaffirms our method's consistent achievement of a total reduction in power usage, exceeding 28.529% at every time step.

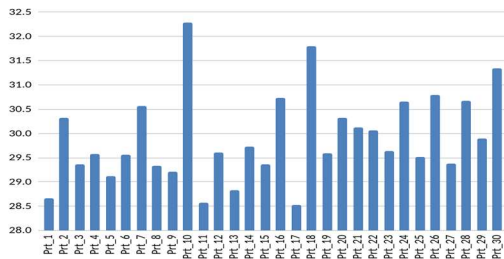


Figure 23. Cumulative Power Usage Reduction Across Devices Over Time.

In summary, the comprehensive data presented in the figures effectively validates our methodology's accuracy, power loss reduction capabilities, and its notable impact on optimizing power usage.

In the third test, we combined both solutions and achieved similar results and advantages from both approaches. However, we also discovered an additional benefit related to the order in which the power factor correction system and the commutation system are applied. After conducting a thorough investigation, we found that if the commutation system applies a new configuration, the power factor correction system does not need to adjust its configuration. Conversely, when the power factor correction system applies a new configuration, the commutation system needs to make adjustments, aligning with our initial prediction.

Table 10 presents the new configuration after implementing the power factor correction system's configuration. It displays the updated settings and values resulting from the combined solution. Additionally, Table 11 focuses specifically on the configuration of the commutation system before and after applying the power factor correction system's configuration. These tables provide valuable insights into the interaction between the two systems and how their configurations influence each other. By understanding this relationship, we can optimize their performance and ensure efficient operation.

Furthermore, we observed a decrease in magnitude due to the reduction in current achieved by the power factor correction system after applying the new configuration. Table 12 showcases the original, optimal, and worst magnitudes before and after implementing the power factor correction system. It also includes the percentage reduction in magnitude for the thirty samples taken. We can observe a magnitude reduction of at least 28.013% in this test, reaching up to 32.421% in some cases. This decrease in magnitude results in reduced system unbalance and subsequently leads to lower power losses.

Table 10. Updated Configuration After Power Factor Correction Integration.

Name	Original				Optimal				Worst			
	I1	I2	I3	Cfg	I1	I2	I3	Cfg	I1	I2	I3	Cfg
Device 1	176.02	105.02	209.87	0	176.02	105.02	209.87	0	176.02	209.87	105.02	1
Device 2	132.32	130.15	193.16	0	132.32	193.16	130.15	1	132.32	193.16	130.15	1
Device 3	214.19	209.15	116.26	0	116.26	209.15	214.19	5	209.15	214.19	116.26	2
Device 4	81.33	133.68	127.67	0	127.67	81.33	133.68	4	127.67	133.68	81.33	5
Device 5	70.04	77.70	164.31	0	164.31	70.04	77.70	4	77.70	164.31	70.04	3
Device 6	108.82	41.24	55.99	0	41.24	55.99	108.82	3	55.99	108.82	41.24	4
Device 7	108.04	186.72	73.19	0	186.72	108.04	73.19	2	108.04	186.72	73.19	0
Device 8	23.68	167.21	193.29	0	167.21	193.29	23.68	3	167.21	193.29	23.68	3
Device 9	145.42	81.35	146.12	0	81.35	146.12	145.42	3	145.42	146.12	81.35	1
Device 10	97.43	21.24	52.13	0	21.24	52.13	97.43	3	52.13	97.43	21.24	4
Sum	1157.29	1153.47	1331.99		1214.35	1214.27	1214.12		1251.64	1647.60	743.50	
Mod	2108.08				2103.14				2198.63			
Avg	1214.25				1214.25				1214.25			
Mod Avg	144.23				0.16				640.93			
Unbalance	11.88				0.01				52.78			

Table 11. Commutation System Configuration Before and After Power Factor Correction Integration.

Optimal Cfg		Worst Cfg	
Before	After	Before	After
0	0	0	1
5	1	0	1
0	5	3	2
5	4	4	5
4	4	2	3
5	3	5	4
0	2	1	0
1	3	2	3
3	3	5	1
0	3	5	4

Table 12. Magnitude Reduction Before and After Power Factor Correction Integration.

Sample	Original Magnitude			Optimal Magnitude			Worst Magnitude		
	Before	After	Reduction	Before	After	Reduction	Before	After	Reduction
Sample 1	2961.50	2108.08	28.82	2957.31	2103.14	28.88	3078.74	2198.63	28.59
Sample 2	2625.42	1819.31	30.70	2424.22	1682.90	30.58	2663.76	1837.85	31.01
Sample 3	2621.55	1844.16	29.65	2619.44	1843.25	29.63	2764.52	1940.88	29.79
Sample 4	2824.71	1982.84	29.80	2821.78	1982.10	29.76	2972.70	2080.87	30.00
Sample 5	2697.44	1906.26	29.33	2666.62	1882.97	29.39	2830.56	2037.63	28.01
Sample 6	3230.23	2270.84	29.70	3201.02	2247.32	29.79	3276.05	2316.31	29.30
Sample 7	3124.99	2160.55	30.86	3109.18	2152.02	30.78	3216.64	2220.78	30.96
Sample 8	2995.32	2106.80	29.66	2990.94	2104.34	29.64	3155.01	2222.18	29.57
Sample 9	2573.50	1809.39	29.69	2556.91	1801.68	29.54	2769.37	1955.09	29.40
Sample 10	2889.46	1952.89	32.41	2888.14	1951.76	32.42	3114.53	2105.82	32.39
Sample 11	2644.32	1882.09	28.83	2640.58	1880.56	28.78	2882.12	2043.38	29.10
Sample 12	2681.83	1878.89	29.94	2657.67	1863.52	29.88	2769.39	1936.72	30.07
Sample 13	2615.15	1853.40	29.13	2537.43	1798.21	29.13	2729.31	1947.78	28.63
Sample 14	2854.66	2008.50	29.64	2833.17	1986.18	29.90	3004.48	2122.92	29.34
Sample 15	2695.52	1899.84	29.52	2690.81	1895.92	29.54	2886.88	2026.62	29.80
Sample 16	2773.74	1919.16	30.81	2762.37	1904.94	31.04	2980.85	2068.88	30.59
Sample 17	2809.61	2004.56	28.65	2801.27	1995.32	28.77	2994.74	2144.72	28.38
Sample 18	3051.21	2076.84	31.93	3024.98	2056.61	32.01	3238.38	2208.31	31.81
Sample 19	3143.73	2209.88	29.71	3108.02	2181.23	29.82	3260.53	2294.21	29.64
Sample 20	2564.45	1781.22	30.54	2560.12	1779.08	30.51	2660.15	1858.78	30.12
Sample 21	2421.04	1678.87	30.66	2378.48	1657.88	30.30	2598.28	1800.86	30.69
Sample 22	2775.91	1938.04	30.18	2764.10	1925.79	30.33	2927.21	2055.06	29.79
Sample 23	2784.01	1955.50	29.76	2768.80	1944.59	29.77	2975.05	2103.10	29.31
Sample 24	2601.99	1793.12	31.09	2579.38	1781.20	30.94	2757.02	1901.44	31.03
Sample 25	2832.24	1970.86	30.41	2768.51	1941.89	29.86	2924.09	2064.60	29.39
Sample 26	2835.29	1957.17	30.97	2834.93	1956.54	30.98	2972.70	2058.80	30.74
Sample 27	2620.19	1845.03	29.58	2618.64	1843.01	29.62	2749.38	1949.83	29.08
Sample 28	2426.81	1680.10	30.77	2369.98	1638.24	30.88	2551.92	1776.40	30.39
Sample 29	3010.29	2103.38	30.13	2994.06	2092.56	30.11	3103.19	2175.91	29.88
Sample 30	2805.17	1920.90	31.52	2799.72	1915.93	31.57	2968.20	2025.65	31.75

6. CONCLUSION

The advent of Industry 4.0 marks a transformative era in industrial operations, characterized by the integration of advanced technologies like IoT, AI, and big data analytics. Central to this transformation is the critical need to enhance energy efficiency and power quality, which our research addresses through innovative approaches in dynamic load balancing and power factor correction. This paper has outlined a pioneering methodology for synergizing these techniques, yielding substantial improvements in energy efficiency and power quality in industrial settings.

Our results demonstrate a promising synergy between dynamic load balancing and power factor correction. This synergy optimizes the configurations of commutation and power factor correction systems, reflecting their interdependence and significant influence on overall performance and energy efficiency. The implementation of these strategies has led to notable reductions in current

magnitude and system unbalance, minimizing power losses and enhancing power quality. In some instances, we observed reductions in magnitude of up to 32.421%.

As Industry 4.0 continues to evolve, the findings from this research are increasingly relevant, offering a practical blueprint for integrating dynamic load balancing with power factor correction strategies. These approaches pave the way for a new paradigm of energy-efficient and high-quality power systems in industrial environments. Future research in this domain is poised to further refine these strategies, potentially integrating with emerging technologies to revolutionize energy management and power quality in the industry.

In conclusion, our study serves as a testament to the transformative potential of harmonizing dynamic load balancing with power factor correction techniques within the Industry 4.0 landscape. It establishes a robust foundation for future research, steering towards a future where industrial operations are characterized by sustainability, efficiency, and optimized power

quality, heralding a new chapter in the annals of industrial evolution.

REFERENCES:

- [1] Y. Lu, "Industry 4.0: A survey on technologies, applications and open research issues," *J. Ind. Inf. Integr.*, vol. 6, pp. 1–10, 2017, doi: 10.1016/j.jii.2017.04.005.
- [2] L. Da Xu, E. L. Xu, and L. Li, "Industry 4.0: state of the art and future trends," <https://doi.org/10.1080/00207543.2018.1444806>, vol. 56, no. 8, pp. 2941–2962, 2018, doi: 10.1080/00207543.2018.1444806.
- [3] P. Leitão, A. W. Colombo, and S. Karnouskos, "Industrial automation based on cyber-physical systems technologies: Prototype implementations and challenges," doi: 10.1016/j.compind.2015.08.004.
- [4] H. Lasi, P. Fettke, H. G. Kemper, T. Feld, and M. Hoffmann, "Industry 4.0," *Bus. Inf. Syst. Eng. 2014 64*, vol. 6, no. 4, pp. 239–242, Jun. 2014, doi: 10.1007/S12599-014-0334-4.
- [5] S. Schneider, "THE INDUSTRIAL INTERNET OF THINGS (IIoT)," *Internet Things Data Anal. Handb.*, pp. 41–81, Feb. 2017, doi: 10.1002/9781119173601.CH3.
- [6] E. G. Popkova, Y. V. Ragulina, and A. V. Bogoviz, *Industry 4.0: Industrial Revolution of the 21st Century*, vol. 1100 AISC. Cham: Springer International Publishing, 2020.
- [7] Y. Naderi, H. Hosseini, G. Zadeh, B. Mohammadi-Ivatloo, J. C. Vasquez, and J. M. Guerrero, "An overview of power quality enhancement techniques applied to distributed generation in electrical distribution networks," 2018, doi: 10.1016/j.rser.2018.05.013.
- [8] F. Zheng and W. Zhang, "Long term effect of power factor correction on the industrial load: A case study," *2017 Australas. Univ. Power Eng. Conf. AUPEC 2017*, vol. 2017-November, pp. 1–5, Feb. 2018, doi: 10.1109/AUPEC.2017.8282382.
- [9] G. Bao and S. Ke, "Load Transfer Device for Solving a Three-Phase Unbalance Problem Under a Low-Voltage Distribution Network," *Energies 2019, Vol. 12, Page 2842*, vol. 12, no. 15, p. 2842, Jul. 2019, doi: 10.3390/EN12152842.
- [10] G. Nota, F. David Nota, D. Peluso, and A. T. Lazo, "Energy Efficiency in Industry 4.0: The Case of Batch Production Processes," 2020, doi: 10.3390/su12166631.
- [11] Y. Zerguit, Y. Hammoudi, I. Idrissi, and M. Derrhi, "A RELAY-BASED AUTOMATIC BALANCING SYSTEM FOR THREE-PHASE LOADS IN INDUSTRY 4.0," *J. Theor. Appl. Inf. Technol.*, vol. 101, no. 5, pp. 2012–2026, Mar. 2023.
- [12] M. Grari *et al.*, "Using IoT and ML for Forest Fire Detection, Monitoring, and Prediction: a Literature Review," *J. Theor. Appl. Inf. Technol.*, vol. 100, 2022.
- [13] M. Yandouzi *et al.*, "Review on forest fires detection and prediction using deep learning and drones," *J. Theor. Appl. Inf. Technol.*, vol. 100, no. 12, pp. 4565–4576, 2022.
- [14] I. Idrissi, M. Azizi, and O. Moussaoui, "A Stratified IoT Deep Learning based Intrusion Detection System," in *2022 2nd International Conference on Innovative Research in Applied Science, Engineering and Technology (IRASET)*, Mar. 2022, pp. 1–8, doi: 10.1109/IRASET52964.2022.9738045.
- [15] Y. Hammoudi, I. Idrissi, M. Boukabous, Y. Zerguit, and H. Bouali, "Review on maintenance of photovoltaic systems based on deep learning and internet of things," *Indones. J. Electr. Eng. Comput. Sci.*, vol. 26, no. 2, pp. 1060–1072, May 2022, doi: 10.11591/IJEECS.V26.I2.PP1060-1072.
- [16] "What is Three Phase System? Definition & Types - Circuit Globe." <https://circuitglobe.com/three-phase-system.html> (accessed Nov. 21, 2021).
- [17] J. B. V Subrahmanyam and E. Engg, "LOAD FLOW SOLUTION OF UNBALANCED RADIAL DISTRIBUTION SYSTEMS," *J. Theor. Appl. Inf. Technol.*, 2009.
- [18] C. K. Chang, S. T. Cheng, and B. K. Boyanapalli, "Three-Phase Unbalance Improvement for Distribution Systems Based on the Particle Swarm Current Injection Algorithm," *Energies 2022, Vol. 15, Page 3460*, vol. 15, no. 9, p. 3460, May 2022, doi: 10.3390/EN15093460.
- [19] "Three Phase Balanced vs unbalanced system / load - TheElectricalGuy." <https://www.theelectricalguy.in/tutorials/three-phase-balanced-vs-unbalanced-system-load/> (accessed Nov. 21, 2021).
- [20] A. S. Leger, D. Smith, J. Spruce, P. Curtiss, G. Gibbons, and M. Miller, "Load management system for tactical microgrids using solid state relays," *2017 North Am. Power Symp. NAPS 2017*, Nov. 2017, doi: 10.1109/NAPS.2017.8107219.

- [21] S. U. Haq, B. Arif, A. Khan, and J. Ahmed, "Automatic three phase load balancing system by using fast switching relay in three phase distribution system," *Proc. - 2018, IEEE 1st Int. Conf. Power, Energy Smart Grid, ICPEGS 2018*, pp. 1–6, Jun. 2018, doi: 10.1109/ICPEGS.2018.8384514.
- [22] I. W. Sutaya, K. U. Ariawan, and I. G. Nurhayata, "The design of automatic three phases load balancing for dynamic electrical installation You may also like The design of automatic three phases load balancing for dynamic electrical installation," *J. Phys*, p. 12002, 2021, doi: 10.1088/1742-6596/1810/1/012002.
- [23] C. M. Coman, A. Florescu, and C. D. Oancea, "Improving the Efficiency and Sustainability of Power Systems Using Distributed Power Factor Correction Methods," *Sustain. 2020, Vol. 12, Page 3134*, vol. 12, no. 8, p. 3134, Apr. 2020, doi: 10.3390/SU12083134.
- [24] B. M. Rija, M. K. Hussain, and A. M. Vural, "Microcontroller Based Automatic Power Factor Correction for Single-Phase Lagging and Leading Loads," *Eng. Technol. Appl. Sci. Res.*, vol. 10, no. 6, pp. 6515–6520, Dec. 2020, doi: 10.48084/etasr.3916.
- [25] K. Alam, L. Sharma, and N. Chopra, "Power Factor Correction for Single-Phase Domestic Loads Using Microcontroller and Triac," *Lect. Notes Networks Syst.*, vol. 151, pp. 91–103, 2021, doi: 10.1007/978-981-15-8218-9_8/COVER.